PNAS RESEARCH ARTICLE | EARTH, ATMOSPHERIC, AND PLANETARY SCIENCES OPEN ACCESS

Vertical conveyor driving the integration of moisture transported by the westerlies to the Asian water towers' atmospheric water cycle

Jing Gao[a,1], Tandong Yao[a,1], Valérie Masson-Delmotte[b], Martin Werner[c], Jean Jouzel[b], Lonnie Thompson[d,1], Mathieu Casado[b], Hans Christian Steen-Larsen[e], Alexandre Cauquoin[f], Ellen Mosley-Thompson[g,1], Zeqing He[h], Rong Cai[h], Taihua Zhang[h], Yigang Liu[a], Gebanruo Chen[a], Baiqing Xu[a], Guangjian Wu[a], Hongxi Pang[i], and Maosheng He[j]

Affiliations are included on p. 10.

Contributed by Ellen Mosley-Thompson; received October 30, 2025; accepted April 10, 2026; reviewed by Raymond S. Bradley and Antje Schwalb

The westerlies moisture transport underpins water security for over two billion people dependent on the Asian water towers (AWTs). However, the mechanisms by which large-scale westerlies-advected moisture is integrated into the AWTs' atmospheric water budget remain poorly understood due to observational gaps. Here, we combine three-dimensional observations of atmospheric water vapor stable isotopes with isotope-enabled modeling. We identify the conveyor mechanism that regulates the vertical moisture transport under calm conditions during the winter-spring period when the westerlies are dominant. Sharp vertical isotopic gradients show that large-scale westerlies-advected moisture is predominantly confined aloft, while local residual moisture persists near the surface. Our results show the interplay of the westerlies' subsidence at night with thermodynamically distinct local residual air, yielding thermal inversions and condensation that suppresses vertical mixing and decouples moisture between the free troposphere and the atmospheric boundary layer. This process constitutes a primary pathway for integrating westerlies-advected moisture into the local moisture budget without precipitation, sustaining near-surface moisture accumulation. Our results provide critical benchmarks for improving atmospheric models, refining climate projections of the intensifying water cycle over the AWTs, and advancing interpretations of isotopic records in regional climatic archives.

the westerlies | moisture transport | water vapor isotopes | atmospheric moisture decoupling | Asian water towers

The Tibetan Plateau (TP, mean elevation > 4,000 m), widely known as the "Asian water towers" (AWTs), exerts major thermal and dynamical influences on climate and supplies freshwater to nearly two billion people (1). These high-altitude water sources are increasingly affected by anthropogenic warming, which is driving pronounced hydrological transitions across the AWTs, including accelerated glacier retreat, diminished snowpack, shifts from snowfall to rainfall, and altered runoff seasonality (2). The region's hydroclimate is shaped by the seasonal interplay between the mid-latitude westerlies, which prevail through October to the following May, and the Indian Summer Monsoon (ISM), which dominate from June to September (2, 3). Although the ISM provides ~70% of the total annual precipitation over the southern AWTs, the westerlies are increasingly recognized as a crucial dynamic regulator of regional hydroclimate. Recent studies emphasized that the westerlies not only dominate the northern and western AWTs (4) but also fundamentally modulate the precipitation seasonality (5) and intensity of the ISM through westerlies–monsoon interactions (6, 7). This further influences premonsoon snow accumulation (8), glacier mass balance (9), and freshwater security (10) in this region. Under rapid warming, changes in the westerlies have been associated with marked spatial heterogeneity in water resources across the AWTs, including a "wet north and dry south" dipole and driving asymmetric lake expansions (10). Accurately constraining the evolving role of the westerlies is therefore essential for understanding and predicting future water resource stability and risk management over the AWTs.

A key unresolved question is how moisture associated with westerlies advection interacts vertically with locally recycled moisture over the AWTs. This question is especially important during the nonmonsoon and premonsoon seasons in the absence of precipitation, when complex topography, boundary-layer processes, and residual moisture can strongly modify the lower atmosphere. Previous studies based on sparse in situ meteorological measurements [such as those from automatic weather stations and radiosondes (11)],

Significance

Recent cryospheric imbalance across the Asian water towers, threatening water security for over two billion people, reflects the coupled effects of large-scale atmospheric circulation and global warming. Disentangling these effects remains challenging due to limited understanding of how moisture advected by the westerlies interacts with local boundary-layer processes. Using three-dimensional observations of atmospheric water vapor isotopes, we trace vertical moisture transport during winter and spring. Combined with modeling, these data reveal a conveyor mechanism that governs vertical moisture transport under calm, westerlies-dominated conditions. Nocturnal subsidence decouples westerlies-advected moisture aloft from residual boundary-layer moisture, locking remote-source vapor into the local water budget. These findings provide key constraints for atmospheric models, climate projections, and interpretations of regional isotope proxy records.

[1]To whom correspondence may be addressed. Email: gaojing@itpcas.ac.cn, tdyao@itpcas.ac.cn, thompson.3@osu.edu, or thompson.4@osu.edu.

This article contains supporting information online at https://www.pnas.org/lookup/suppl/doi:10.1073/pnas.2529749123/-/DCSupplemental.

reanalysis products (7) and high-resolution model simulations (12) have clarified broad contrasts between monsoonal and westerly regimes, but they have not directly resolved the vertical interaction between westerlies advection and local residual moisture. A fundamental challenge in alpine meteorological research lies in integrating discontinuous field measurements, acquired across diverse locations and seasons, and scarce vertical profiles. To bridge these spatiotemporal gaps, we utilize stable isotopes in atmospheric water vapor (δD_v and d-excess$_v$ = $\delta D_v - 8 * \delta^{18}O_v$). Previous studies have documented that such thermodynamic history is incompletely preserved in stable isotopes in precipitation ($\delta^{18}O_p$, δD_p, and d-excess$_p$) at synoptic scale (13–15). δD_v and d-excess$_v$ further encodes the continuous thermodynamic history of an air mass from initial evaporation to final condensation across varying timescales (16).

To accurately capture the dynamics of this atmospheric interaction, here we combine unprecedented 32 vertical profiles of the atmospheric water vapor isotopic composition and meteorological variables, using a helium-tethered balloon platform (called "Jimu Balloons", *SI Appendix*, Fig. S1), with simultaneous surface vapor isotopic measurements (δD_{sv} and d-excess$_{sv}$ at 2 m above the ground level (AGL)]. These observations were obtained during the westerlies-dominated seasons (December to May, 2017–2019) at two sites, Lulang (3,335 m a.s.l) and Nam Co, [4,730 m a.s.l, ~377 km to the north, see *Materials and Methods*) (Fig. 1*A*). Lulang, located in the southeastern TP near the Yalung Tsangpo moisture corridor, is strongly influenced by moisture transport from the Bay of Bengal and the Indian Ocean, whereas Nam Co is a high-altitude inland lake basin, strongly influenced by seasonal monsoon–westerlies alternation. Comparisons of the observations from these two sites allow us to evaluate whether the mechanisms inferred from the vertical isotopic profiles are persistent across different surface conditions over the southern AWTs.

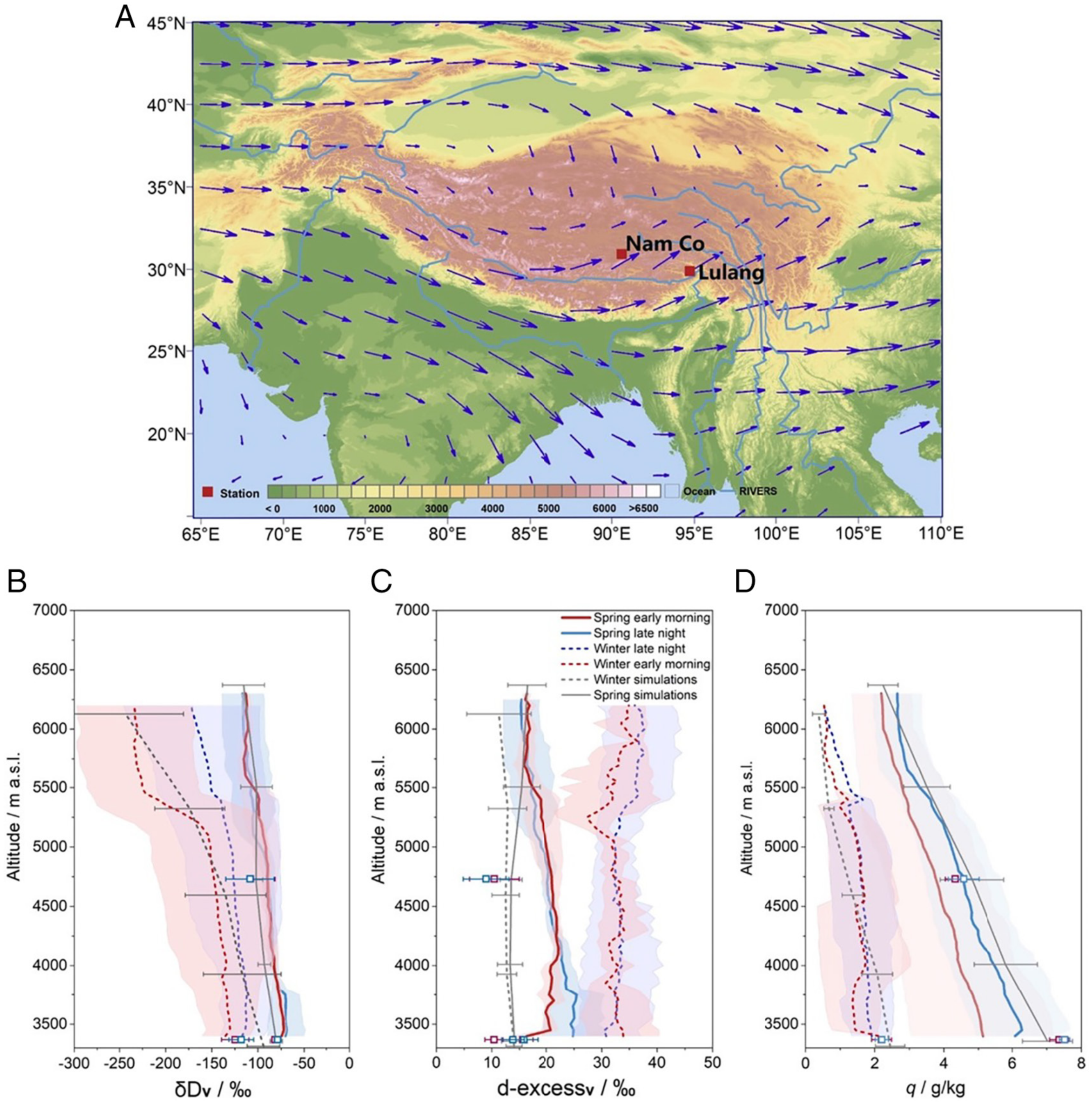

Fig. 1. Regional moisture transport pattern and vertical profiles of atmospheric water vapor stable isotopes and specific humidity (*q*) from observations and ECHAM6-wiso model simulations. (*A*) Climatological moisture transport patterns in winter and spring (1978–2019) from ERA5 reanalyses (blue vectors). Red squares show locations of in situ atmospheric water vapor stable isotope measurements at Lulang and Nam Co. (*B*) Observed vertical profiles of δD_v at Lulang in winter and spring (colored lines with shading), compared with corresponding ECHAM6-wiso model simulations (gray lines) and simultaneous surface observations (squares). Blue profiles and squares represent late-night conditions (averaged from all ascending vertical profiles within the respective time window; *SI Appendix*, Fig. S1), while red profiles and squares represent early-morning conditions (averaged from all descending vertical profiles). Winter data represent January 2019 averages; spring data represent April 2019 averages at Lulang. (*C*) same as (*B*), but for vertical profiles of d-excess$_v$. (*D*) same as (*B*), but for specific humidity (*q*). Vertical profiles at Nam Co in spring are shown in *SI Appendix*, Fig. S4.

To maximize comparability of two sites and different seasons, all profiles were measured from 10 pm to 10 am local time, when the atmosphere boundary layer (ABL) is shallowest. We interpret these measurements using a state-of-the-art isotope-enabled general atmospheric circulation model [ECHAM6-wiso (17)], nudged to ECMWF reanalysis data, along with theoretical models (Rayleigh distillation, the mixed cloud isotopic model referred as MCIM and a mixing process model, described in *Materials and Methods* and *SI Appendix,* Fig. S2). This framework provides a unified, process-based picture by identifying vertical structures of atmospheric moisture and linking them to a nocturnal subsidence-driven decoupling between the westerlies advection in the free troposphere and the local residual air within the ABL.

Results

Vertical Profiles of Water Vapor Stable Isotopes. Averaged vertical profiles of δD_v and d-excess$_v$ at both Lulang and Nam Co reveal strongly stratified atmospheric moisture layers governed by large-scale circulation (Fig. 1). A pronounced seasonal contrast emerges between winter and spring. At Lulang, monthly δD_v is more than 50‰ lower in winter than in spring (Fig. 1*B*), whereas d-excess$_v$ is increased by ~15‰ (Fig. 1*C*). This isotopic contrast is strongly tied to changes in large-scale westerlies advection across the southern AWTs [*SI Appendix,* Fig. S3, (18)]. Above 2,100 m at Lulang (hereafter all the altitudes refer to ground level), vertical isotope gradients exceed the seasonal variability observed in near-surface water vapor isotopes (δD_{sv} and d-excess$_{sv}$) (19). In January, averaged δD_v above ~2,000 m is depleted by ~80‰ relative to values below 1,700 m, whereas d-excess$_v$ displays an inverse change of ~5‰. Because extremely strong winds and low temperatures prevented balloon operation, winter profiles are unavailable at Nam Co. Accordingly, the winter-to-spring contrast is constrained primarily by the Lulang observations and is most representative of the calm conditions under which the profiles were obtained.

Spring profiles nevertheless show similar vertical structures of atmospheric moisture with those in winter. In April, δD_v is enriched below ~700 m at Lulang and decreases above this elevation, and differences in δD_v between late-night and early-morning profiles are much smaller than those in winter (Fig. 1*B*). The d-excess$_v$ values are ~20‰ lower in spring than those in winter above ~1,800 m, and it decreased by ~5‰ at the lowest ~500 m in the early morning compared to the late night (Fig. 1*C*). The vertical variations in δD_v in May at Nam Co are consistent with those at Lulang in April at comparable heights above the surface. Differences in d-excess$_v$ between Lulang and Nam Co (~5‰, peak to peak) are confined to the surface only up to ~500 m (*SI Appendix,* Fig. S4). Near-surface diurnal variabilities in δD_{sv} and d-excess$_{sv}$ are strongly attenuated (~75%) compared to the full vertical profiles (*SI Appendix,* Fig. S5), indicating substantial vertical difference of atmospheric moisture. These measurements provide a vertically resolved documentation of moisture stratification across the AWTs. Previous studies were restricted to either near-surface measurements or lacked sufficient vertical resolution to capture this atmospheric feature (20, 21).

Humidity profiles support this isotope-based interpretation. q decreases nearly linearly with height in all months, and April–May values exceed January values throughout the atmospheric column (Fig. 1*D*). ECHAM6-wiso model successfully capture the observed vertical variations in δD_v at both sites (Fig. 1*B*), but it systematically underestimates the amplitude of d-excess$_v$ variability (Fig. 1*C*). Together, these results identify a vertically organized moisture structure that varies systematically with season and elevation.

Isotopic Transitions Identify the Atmospheric Stratification. Empirical orthogonal function (EOF) analysis resolves the vertical atmospheric structure (*SI Appendix,* Fig. S6). At Lulang, the first two EOF modes account for 93% of the total variance in both δD_v and d-excess$_v$. Using d-excess$_v$ transitions, we identified the ABL boundaries at ~600 m in winter and ~900 m in spring at Lulang. The ABL boundary identified from d-excess$_v$ is typically 100 to 300 m higher than those inferred by δD_v. These isotopically defined transitions agree closely with previous documented ABL heights of ~460 ± 100 m in winter and ~600 ± 200 m in spring at Lulang (22). Nam Co displays a similar spring ABL transition at ~750 m, indicating that this stratification is regionally coherent.

The stratified atmosphere structure is more clearly revealed when daily fluctuations tied to weather variations are filtered out prior to vertical profile compositing (See the details in *Materials and Methods*). The most pronounced fluctuations in δD_v and d-excess$_v$ together with divergences between late-night and early-morning profiles, represent the distribution of the free troposphere above ~1,600 m in winter and ~1,800 m in spring at Lulang (Fig. 2 *A–D*). Between the free troposphere and the ABL, a mixed layer extends from ~600 to 1,600 m and is characterized by minimal vertical variances in δD_v and d-excess$_v$ and vertically homogeneous q under stable atmospheric conditions (Fig. 2 *E* and *G*). The surface layer, occupying the lowest portion of the ABL (below 100 m at Lulang), exhibits the steepest gradients in isotopes, q and air temperature (T), and the largest diurnal variability of meteorological parameters within the ABL (*SI Appendix,* Fig. S7).

Comparisons of spring vertical profiles between Lulang and Nam Co confirm these elevation-dependent stratifications, although the free troposphere descends to ~1,400 m at Nam Co. Such fluctuations in ABL height over the AWTs are corroborated by operational meteorological soundings (18), and simulations from the ECHAM6-wiso model which successfully reproduces the isotopically defined vertical structures at both sites (*SI Appendix,* Fig. S6). The systematic seasonal elevation differences in transition heights (~200 m) are consistent with thermal expansion of the atmospheric column and enhanced premonsoon convective activity.

The isotopically defined mixed layer structure cannot be resolved from thermodynamic profiles alone. During nocturnal periods in both winter and spring, T, q, or potential temperature (PT) decreases monotonically with elevation (Fig. 2 *E–H* and *SI Appendix,* Fig. S7), obscuring the layer boundaries that are evident in the isotope profiles. Notably, δD_v and d-excess$_v$ profiles show systematic early-morning depletion relative to later-night values, particularly within the free troposphere and ABL, coincident with decreased q and T.

These isotopic stratifications likely reflect vertical moisture interactions between large-scale advection and local residual air, modulated by kinetic fractionation processes during phase transitions (23, 24). Condensation preferentially results in depleted δD_v (δD_{sv}) in air above the mixed layer and near the surface. Persistent clouds aloft and surface frost formation in early morning support this. We further examine the role of the westerlies transport in regulating this atmospheric stratification in the following section.

The Westerlies Subsidence Characterized with δD_v and d-excess$_v$ Variations. To understand how the westerlies moisture transport contributes to such atmospheric stratification over the southern AWTs, we combined the isotope-enabled ECHAM6-wiso simulations with in situ observations. The observations show that local δD_p generally exceeds both δD_v and δD_{sv}, whereas

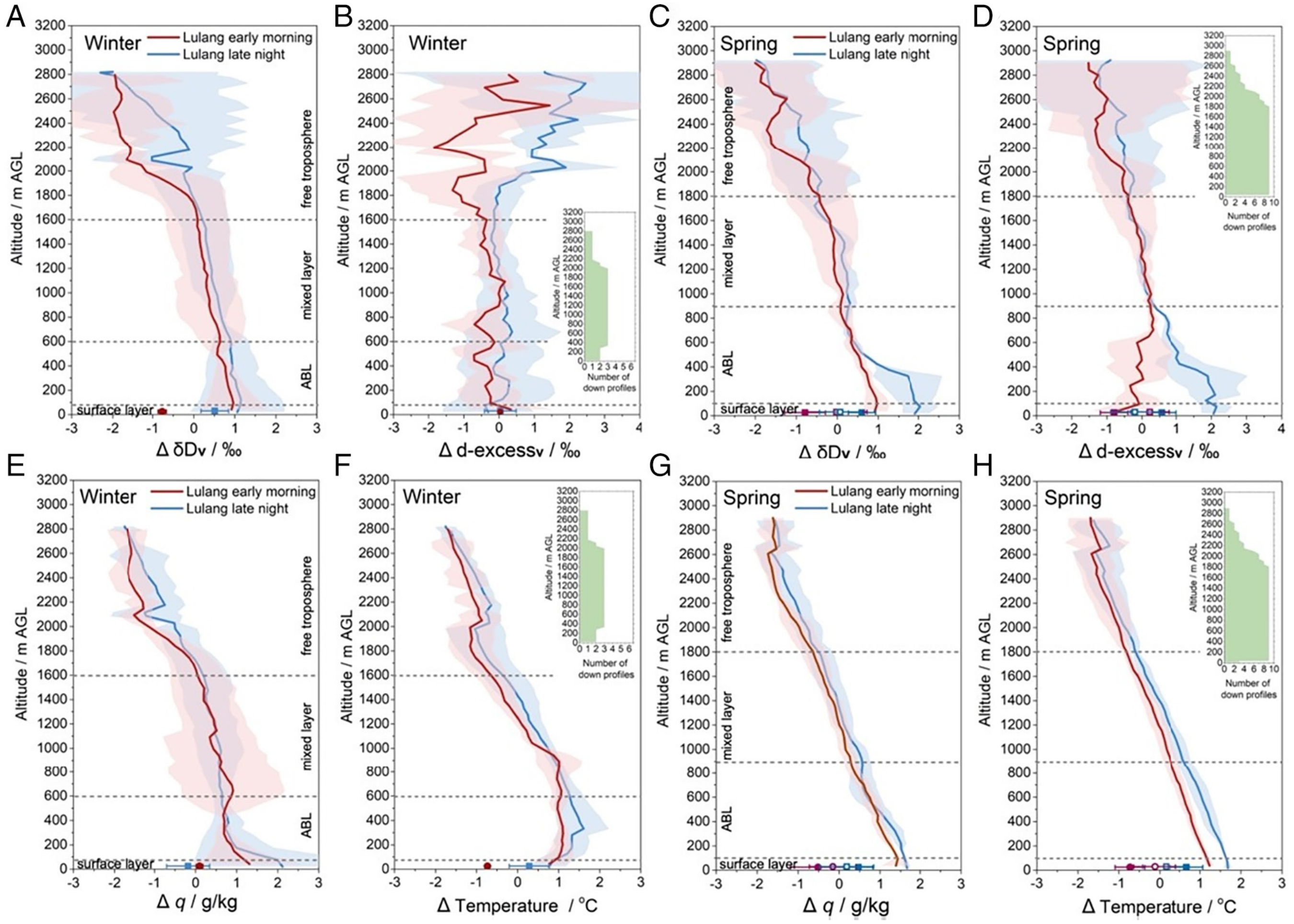

Fig. 2. The stratified atmospheric structure in winter and spring as identified by observed atmospheric water vapor isotopes and meteorological parameters. Vertical profiles of δD_v, d-excess$_v$, specific humidity (*q*), and air temperature were filtered to remove day-to-day noise prior to compositing the anomalies. (*A*, *B*) Winter δDv and d-excessv profiles at Lulang, (*C*, *D*) Spring δDv and d-excessv profiles at Lulang. (*E*) same as (*A*), but for specific humidity; (*F*) same as (*A*), but for air temperature. (*G*) same as (*C*), but for specific humidity; (*H*) same as (*C*), but for air temperature. Blue profiles represent late-night conditions (averaged for all ascending vertical profiles within the respective time window, *SI Appendix*, Fig. S1), while red profiles represent early-morning conditions (averaged for all descending vertical profiles). Horizontal scatter points show surface observation anomalies calculated relative to daily averaged surface values. Shaded envelopes represent ±1 SD based on observational magnitudes. Green bar plots indicate the number of validated profiles used for profile generation at each altitude. The y-axis shows altitude above ground level (AGL) for each site. Ground-level elevations are 3,335 m a.s.l. at Lulang. Horizontal gray dashed lines delineate atmospheric stratification boundaries from the surface layer to the base of the free troposphere for Lulang. For Nam Co, no winter observations were made but spring observations indicate that the boundary layer is suppressed to 750 m AGL, the bottom of the free troposphere extends down to 1,400 m AGL and the mixed layer is located in between (shown in *SI Appendix*, Fig. S4).

d-excess$_p$ falls within the range of d-excess$_v$ and d-excess$_{sv}$ at both Lulang and Nam Co (*SI Appendix*, Fig. S5). This reflects a partial overlap between moisture sources of precipitation and those of contemporaneous atmospheric water vapor.

Changes in the monthly moisture flux patterns provide mechanistic support for our interpretation of enriched δD_v and decreased d-excess$_v$ in the free troposphere in April at Lulang compared to January. In January, the westerlies transport moisture from northeastern Iran, the North Atlantic, and southern Himalayas into the upper free troposphere over the AWTs (25). The cold and dry ice margin or mixed-phase cloud processes (26) cause kinetic fractionation (15) and yield markedly depleted δD_v and elevated d-excess$_v$ in the upper troposphere. These features substantially differ from isotopic signals arising from local surface evapotranspiration.

In April, by contrast, large-scale advection transports warm and moist air masses from the Bay of Bengal (BoB) and southern Himalayas to Lulang (*SI Appendix*, Fig. S3). As the westerlies shift northward in spring, the vertically integrated moisture flux strengthens further in May, transporting increasingly warm and moist air masses from the tropical Indian Ocean across the Himalayas into the upper troposphere over the southern AWTs (27). This enhanced moisture transport is associated with enriched δD_v and reduced d-excess$_v$ in the free troposphere (Fig. 1 *B* and *C*). Compared to long-distance transported moisture, oceanic evaporation and continental moisture recycling (26) yield exceptionally high δD_v and correspondingly lower d-excess$_v$ (28), consistent with observations from the EUREC^{4}A campaign over the western tropical Atlantic (29) (*SI Appendix*, Fig. S8). ECHAM6-wiso simulations further verify intense local evapotranspiration during these months, contributing to enriched δD_v within the ABL (*SI Appendix*, Fig. S9). Most ABL profiles exhibit an enriched δD_v flux relative to the mixed layer and free troposphere, consistent with the expectation of preferential release of heavy isotopologues to vapor by local evapotranspiration. Nam Co, located in the central AWTs, receives proportionally more moisture from continental recycling and local evaporation (30) than Lulang, resulting in its lower d-excess$_v$ (*SI Appendix*, Fig. S4).

A robust link emerges between the vertical positioning of the westerlies and isotopic structures in the free troposphere at both sites. We tracked the altitudes of the maximum westerly jet speed over Lulang during our observation periods, using ECHAM6-wiso simulations (Fig. 3 *A* and *E*). This analysis shows a systematic subsidence of the westerlies from the late night to early morning under calm and clear conditions (Fig. 3 *I* and *J*). Over Lulang, strong downward vertical fluxes in the free troposphere coincide with substantial decreases in q (~0.5 g/kg) and depletion in δD_v (20 to 80‰) from late night to early morning (Fig. 3 *B–G*). A typical case occurred on 21 January 2019, when δD_v decreased by –80‰ and q declined by ~1 g/Kg between 2,900 m and 2,100 m within 1 h. Weaker downward vertical fluxes occurred within the ABL and were accompanied by stronger dehydration but less δD_v depletion.

The subsidence is also reflected in d-excess$_v$. At Lulang, d-excess$_v$ decreases by ~2.5‰ on average in winter but increases by ~3‰ in spring within both the free troposphere and the ABL (Fig. 3 *D* and *H*). Conversely, Nam Co exhibits opposite late-night to early-morning variations in q, δD_v, and d-excess$_v$ within the free troposphere and ABL (*SI Appendix,* Fig. S4), reflecting stronger decoupling between atmospheric humidity and isotopic signatures. Further independent evidence for subsidence comes from the free descent of our Jimu balloon at ~2,000 m within 2 h (*SI Appendix,* Fig. S10). This resembles nocturnal radiative cooling and large-scale descent as documented in the inner Sahel and Chilean Andes (31, 32). These results demonstrate that the westerlies subsidence shapes the nocturnal water vapor isotopic heterogeneity across the atmospheric column over the southern AWTs.

To understand whether vertical exchange of moisture occurring during the westerlies subsidence, we analyzed the averaged diurnal variations in vertical profiles and corresponding surface measurements of δD_{sv} and d-excess$_{sv}$ in both winter and spring (*SI Appendix,* Fig. S11). Persistent differences between vertical profiles and surface measurements for hourly δD_v and d-excess$_v$ indicate that moisture from different sources undergoes incomplete vertical mixing during the westerlies subsidence, and kinetic fractionation effects play a nonnegligible role in shaping isotopic stratification. This interpretation is further supported by heterogeneous humidity variations observed in vertical profiles and near-surface measurements (*SI Appendix,* Fig. S11). Because kinetic fractionation depends on changes of climatic conditions (such as air T, q, and wind speeds) (16), we further evaluated these controls statistically. Principal component analyses indicate that local air T, q, and wind speed collectively explain up to 67% of δD_v variance in the free troposphere, but less than 40% within the ABL. Nevertheless, the most robust δD_v-T correlation in spring near the surface at Lulang (0.79‰/°C, R = 0.69, $P < 0.01$)

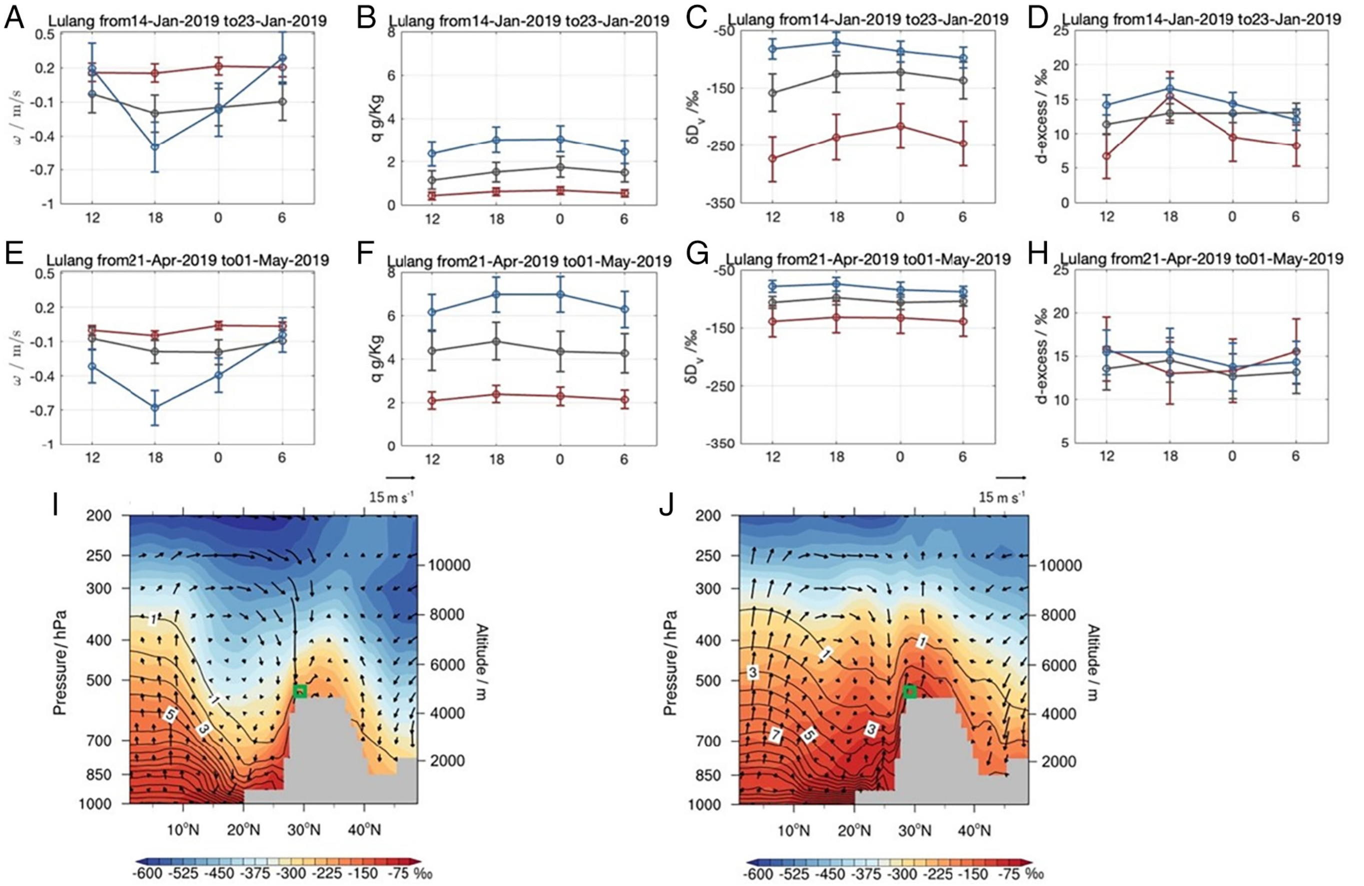

Fig. 3. Nocturnal westerlies subsidence and vertical moisture transport patterns during our observation periods from ECHAM6-wiso model simulations. (*A*–*H*) Diurnal variations in vertical wind velocity (w), specific humidity (q), δD_v, and d-excess$_v$ at various atmospheric levels. (*A* and *E*) Mean vertical wind velocity (w, m/s) at 6-h intervals within the atmospheric boundary layer (ABL, 650 hPa), mixed layer (550 hPa), and free troposphere (450 hPa) for Lulang (January 14–23 and April 21–May 1, 2019). To ensure the model data are representative of the values at the observation sites, vertical wind velocities were calculated as a spatial average of 3 × 3 grid (the nine grid cells centered on each site). Positive values indicate downward air mass movement (subsidence); negative values indicate upward movement. Error bars represent ±1 SD across the data at 6-h intervals. (*B* and *F*) Corresponding specific humidity (q, g/kg) profiles for the same periods and locations as panels *A*, and *E*, respectively. (*C* and *G*) Corresponding δD_v (‰) profiles for the same periods and locations as panels *A* and *E*, respectively. (*D* and *H*) Corresponding d-excess$_v$ (‰) profiles for the same periods and locations as panels *A* and *E*, respectively. Error bars in panels *B*–*L* represent ±1 SD across the respective 6-hour time intervals. Integrated vertical moisture flux (vectors, kg m^{-1} s^{-1}) overlaid with q contours (gray lines, g/kg) and δD_v (color background shades, ‰) during nocturnal periods (00:00 to 06:00 local time) for January (*I*) and April (*J*), within the 90 to 95°E longitude band. Green squares indicate the location of the Lulang observation site.

points to a significant influence of kinetic effects (33) within the ABL. Therefore, we suggest that a nocturnal westerlies subsidence promotes decoupling between the ABL moisture and the westerlies-advected moisture aloft.

Decoupling of Westerlies-Advected Moisture From ABL Moisture. Our vertical profiles and ECHAM6-wiso simulations reveal that the westerlies advection transports remote air masses into a relatively warm, moist local atmosphere in both winter and spring. This process enhances aridity aloft in the early morning and promotes condensation in the upper mixed layer during westerlies subsidence. Concurrently, nocturnal surface radiative cooling suppresses local shallow convection (11), and weakens upward moisture transport within the ABL. Consequently, two persistent thermal inversion layers develop, one within the upper ABL and the other atop the mixed layer, with maximum temperature gradient of 0.27 °C/10 m ($R^2 = 0.86$, Fig. 2 *F* and *H*). These inversion layers act as barriers between thermodynamically distinct air masses and sharply reduce vertical moisture exchange between large-scale advection and local ABL residual air, particularly at Lulang in January.

Probability Density Function (PDF) analysis of our in situ vertical profiles reveals a complete decoupling between the local boundary layer and the free troposphere. The significantly depleted δD_v and low mixing ratios observed in winter are tightly constrained by Rayleigh distillation, contrasting sharply with the spring PDF distributions. At lower altitudes, the PDF density cores align closely with the MBL mixing curve, whereas those in the free troposphere cling tightly to the Rayleigh distillation curves (Fig. 4). The stretched late-night density cores confirm the dominance of cold, dry westerlies subsidence within the free troposphere, while early-morning cores concentrate at lower altitudes, shifting toward the mixing curve. This reflects a clear diurnal shift in the atmospheric dynamics. These provide robust evidence of the vertical isotopic decoupling.

This decoupling arises through four-linked processes: 1) the westerlies subsidence generates strong thermal inversions that suppress vertical moisture mixing, 2) these inversions physically isolate moisture in the free troposphere from the ABL, and 3) upward transport of moisture evaporated in the ABL leads to condensation, forming an inversion cap at the upper ABL, and 4) condensation at inversion interfaces further strengthens the barrier by releasing latent heat and enhancing static stability. Nocturnal evolution of δD_v and d-excess$_v$ peaks within the ABL indicate progressive moisture subsides from late night to early morning, coinciding with ~100 m thinning of the nocturnal ABL during our observation periods (Fig. 2 *A–D*). Such early-morning ABL thinning has been inferred previously from meteorological sounding observations in this region (18). In the mixed layer, reduced vertical gradients of δD_v and d-excess$_v$ with altitude and T indicate effective isolation of the free troposphere from the ABL. This is conducive to a closed moisture budget without moisture input from the local ABL. Under this condition, Rayleigh distillation and MCIMs reproduce the observed δD_v-T and δD_v-q relationships, supporting the inference that oceanic-source moisture is advected into the free troposphere over the southern AWTs in both winter and spring.

The decoupling also modulates the δD_v-q relationship by separating moisture sources and kinetic effects between the free troposphere and ABL. In winter, westerlies-transported moisture from BoB reaches to Lulang through Rayleigh distillation in the free troposphere, driving late-night δD_v variations (Fig. 4*B*). Low temperatures and mixed-phase cloud processes along these oceanic-to-plateau transport pathways generate elevated d-excess$_v$ (>40‰ above ~2,000 m AGL) in the free troposphere. Concurrently, near-surface condensation regulates ~50‰ depletion of average δD_{sv} between early morning and late night. The spring decoupling resembles with those in winter, but mixing between BoB-source moisture and dry westerlies-advected moisture exerts a stronger influence in the free troposphere (Fig. 4*C*), as derived from a mixing model (34). The aloft condensation can well explain the significant early-morning depletion within the ABL at Lulang. However, the stronger contribution of local evaporation and weakened influence from moisture aloft intensifies the decoupling.

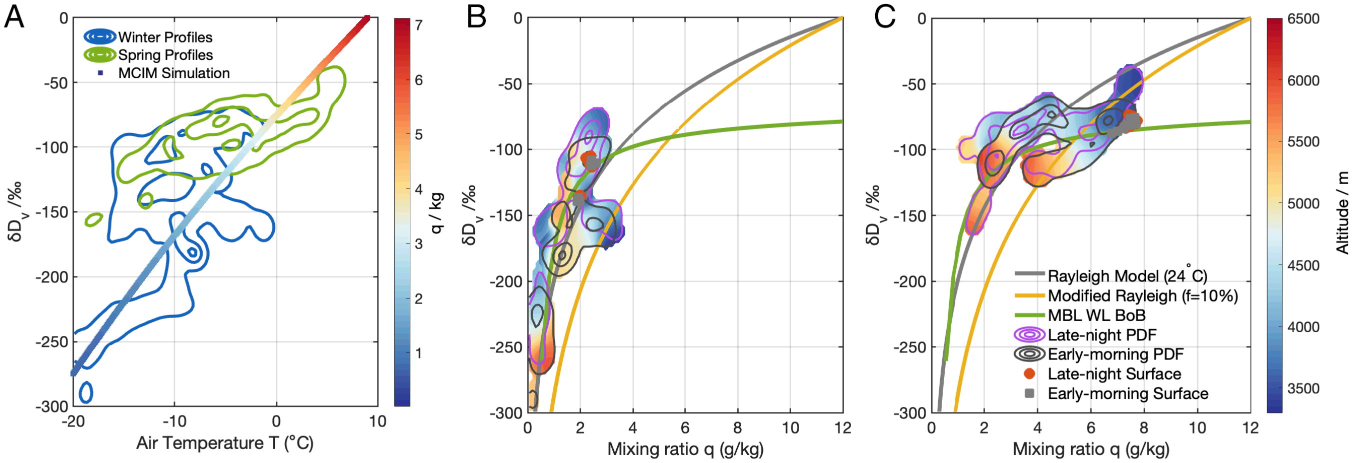

Fig. 4. The decoupling processes in atmospheric water vapor stable isotopes from the ABL to free troposphere. (*A*) Evolution of δD_v as a function of corresponding air T and q for in situ vertical profile observations compared with MCIM simulations (straight colored line) along a cooling trajectory with supersaturation function (*Materials and Methods*). Contours present the 2D probability density of δD_v in winter (blue) and spring (green) at Lulang, using Probability Density Functions. The color bar represents specific humidity (g/kg). (*B*) Nocturnal evolution of δD_v and δD_s in winter at Lulang as a function of q to distinguish multisource moisture characteristics and mixing processes. Contours show 2D probability density of δD_v at late night (solid purple lines) and early morning (solid dark gray lines), enclosing the altitudes where the vapor retained the most time (the probability density cores). Colored background mapping represents the density-weighted altitude (m a.s.l.). Color curves show Rayleigh distillation (gray and yellow) and mixing model simulations (green). The Rayleigh distillation simulations indicate condensation and rainout in an open system, while the mixing model simulations indicate physical mixing of different air masses (*Materials and Methods*). The corresponding surface observations were shown as scatters. (*C*) same as (*B*), but for spring observations at Lulang. The color bar represents altitude (m a.s.l.). In the legend, the following acronyms are used: MBL (the water isotopic Marine Boundary Layer model[36]), WL (westerlies), BoB (Bay of Bengal), PDF (Probability Density Functions).

Thus, a clear decoupling mechanism emerges in both winter and spring (Fig. 5). During the day, surface heating expands the ABL to ~1,500 to 4,000 m AGL (18), and enhances turbulence mixing and upward moisture transport. At night, surface radiative cooling and the westerlies subsidence drive downward transport of daytime convective moisture, whereas upward fluxes of locally surface-evaporated moisture weaken, associated with latent heat release and condensation near the top of ABL. The nocturnal inversion layers occur nearly every night, producing rapid humidity changes that promote phase transitions when thermodynamically distinct air masses interact. The sharp gradients in δD_v and d-excess$_v$ observed at layer interfaces are consistent with this process, as condensation preferentially removes heavy isotopes from the remaining vapor.

Local surface conditions further modulate these dynamics and explain site-specific differences. Dense forests at Lulang and open lake surface at Nam Co act as nighttime warm pools relative to surrounding meadows and glaciers, providing substantial evaporative moisture with enriched δD_v into the ABL. In spring, a higher and more stable nocturnal ABL with stronger inversion layers above the mixed layer is observed at Lulang, whereas strong nocturnal winds at Nam Co reduce sensible heat flux and accelerate ABL thinning. The surface condensation further inhibits upward vertical moisture transport within the ABL (Fig. 5), maintaining a near-steady atmosphere beneath, similar to conditions observed at Summit Camp, Greenland (35). The presence of surface frost and low-level clouds in the early morning supports this interpretation.

Under these conditions, the free-tropospheric moisture is condensed and integrated into the local water cycle through phase transitions at night, while the near-surface atmosphere remains thermally isolated and retains moisture accumulation. We estimate that ~30% of the simultaneously advected free-tropospheric flux is integrated into the local atmospheric water cycle through this nocturnal vertical conveyor. This represents the primary pathway for net westerlies moisture input. Under calm conditions, the strengthened thermal inversions are both a product and a driver of these vertical moisture transports. ECHAM6-wiso simulations further reveal that the westerlies moisture contributes ~34% of the annual moisture flux at both sites. This flux has intensified significantly during 1979–2020, increasing by ~4×10^6 kg/m/y. This enhanced moisture input into the ABL would therefore be expected to directly modulate atmospheric humidity, cloud cover, and energy balance, with profound implications for glacier mass balance and regional water availability.

Conclusion and Future Implications

Our results show that vertical isotopic profiles of atmospheric water vapor are powerful indicators for understanding atmospheric dynamical processes over the AWTs. Using accurate three-dimensional observations of isotopic compositions of atmospheric water vapor, combined with isotope-enabled atmospheric modeling, we find that dual conveyor mechanisms drive vertical moisture transport, with westerlies-advected moisture dominating the free troposphere and locally sourced moisture shaping the boundary layer at diurnal scale. Our findings further reveal a mechanistic link among westerlies advection, moisture sources, and the local diurnal atmospheric water cycle. Nocturnal westerlies subsidence strengthens inversion-layer isolation and promotes hydrological decoupling between the large-scale westerlies advection and local residual air. This appears to be a primary pathway for incorporating westerlies-advected moisture into the local moisture budget under cold-surface or calm-weather conditions. This connection persists throughout three-quarters of the year, particularly without the influence of Indian summer monsoon when the westerlies remain the dominant moisture driver (1, 10). This connection is strongest during dry seasons and in arid environments.

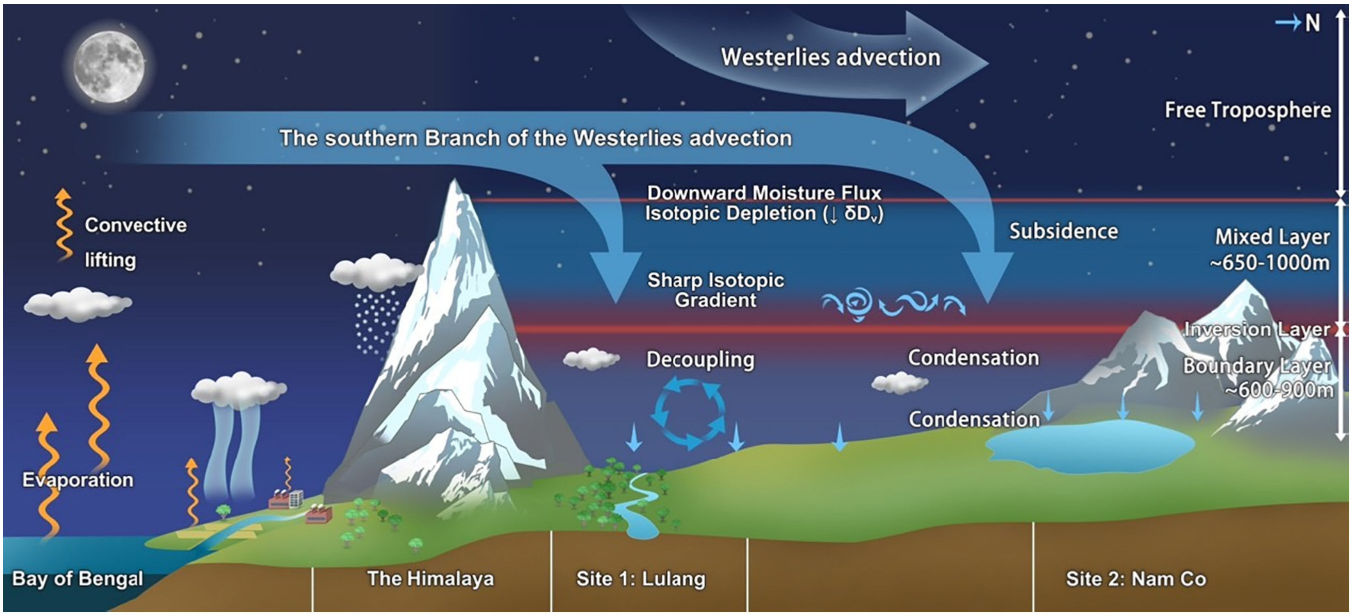

Fig. 5. Schematic illustration of the decoupled conveyor mechanism driving the vertical integration of moisture advected by the westerlies into the atmospheric water cycle on the AWTs. Cold westerlies advection (blue) interplays with relatively warm and wet residual air. The interplay between these two distinct air masses yields a mixed layer (light blue) and an inversion layer (dark red) just above the boundary layer (light purple). The decoupling of moisture within the boundary layer isolates residual air (circled blue arrows). In spring, the heights of ABL and mixed layer are higher than those in winter at Lulang, associated with the northward reduction of the westerlies advection. Orange twisted arrows indicate surface evaporation and evapotranspiration, and small blue straight arrows indicate condensation. The mean height of the different layers is indicated including in both winter and spring. The extended free troposphere subsides to ~1,400 m AGL at Nam Co in spring, which is about 400 m lower than that at Lulang, while a shallower mixed layer at Nam Co than Lulang because of the strong nocturnal winds and vast basin at Nam Co.

A limitation of this study is that the balloon observations were obtained only under relatively calm conditions, so the dataset may underrepresent periods of strong synoptic conditions. Accordingly, our conclusions are best interpreted as identifying persistent mechanisms under calm-weather conditions rather than fully characterizing all synoptic regimes across the annual cycle.

These findings have broader implications for hydroclimatic change over the plateau. In recent decades, westerlies moisture flux has increased in winter and spring (36), and evapotranspiration over India, Bangladesh, and the southern AWTs has increased (*SI Appendix*, Fig. S12). These suggest that the changes in the regional water cycle across the plateau will depend on the shifts in the moisture sources, the changes in vertical conveyors, and in the decoupling process related to westerlies subsidence. This challenges the assumption that moisture carried by cold and dry westerlies from the remote North Atlantic plays an important role on AWTs' water budget (37).

Our findings provide a framework for linking present-day vertical moisture transport to both paleoclimate interpretation (such as regional ice cores, tree ring) and future hydroclimate projection. Our analysis shows that free-tropospheric moisture in winter and spring commonly retains upstream signatures from oceanic or south-Himalaya continental sources, whereas near-surface moisture is primarily influenced by local residual air, associated with pronounced variations in δD_v and d-excess$_v$. It implies the need for more quantitative interpretation of how westerlies-advected moisture is recorded in regional ice-core isotope archives, which integrate a complex hydrological and isotopic budget. Incorporating water vapor isotopes into higher-resolution climate models, and using our dataset against observations and ice core records, has the potential to substantially enhance our understanding of past moisture transport dynamics toward the AWTs over glacial-interglacial timescales (38, 39) and reduce uncertainty in future projections under continued warming. Expanded integration of aerial, surface, and satellite observations will be critical for resolving the full three-dimensional moisture transport in high-altitude regions and for improving future hydroclimatic monitoring, forecasting, and prediction.

Materials and Methods

Two In Situ Observation Locations. The in situ measurements of vertical profiles of atmospheric water vapor stable isotopes and simultaneous meteorological data were retrieved at Lulang. The Lulang site (29.76°N; 94.74°E; 3,335 m a.s.l.) is located in a south-north oriented mountain valley in the northern Himalayas close to the Yalung Zangbo River and in the crucial channel of moisture transport toward the interior AWTs from the Indian Ocean by the southern branch of the westerlies or Indian monsoon. The regional climate is semihumid, with an annual average precipitation of 800 to 1,000 mm (~70% falling during the summer monsoon), while the annual average relative humidity is 73.5%, and the annual average air temperature is 5.5 °C (40). High air temperatures and precipitation predominantly occur from June to September, and less than 1 m of snow falls in spring. Mixed forests, alpine shrubs, and meadows are prevalent within the river valley to 4,400 m (41).

Our in situ measurements were also implemented in May 2019 at Nam Co (30.77°N, 90.98°E, 4,730 m a.s.l.), located on the southeastern shore of the Lake Nam Co on the southern TP. The surface area of the lake was ~2,015 km^2 in 2004 with a maximum depth of 99 m. The annual mean air temperature is ~0 °C and the annual mean precipitation is ~450 mm, with 91% of precipitation occurring from May to September (42). Most inflow is distributed along the western and southern shores of the lake during the summer season dominated by the Indian Summer Monsoon (42) and is primarily controlled by precipitation and glacier meltwater. Mean annual evaporation over the lake surface is close to 790 mm and 320 mm over the catchment (43). The Indian monsoon dominates atmospheric moisture transport, while the cold and dry westerlies dominate in the other seasons. Alpine meadow and steppe grasses are prevalent in the catchment in summer, while desert soils surround the lake in other seasons. The total surface area of glaciers above 5,300 m a.s.l. in the Nam Co basin is 200 km^2, particularly in the northern Nyainqentanglha Mountains (44).

In Situ Measurements of Atmospheric Water Vapor Stable Isotopes. There are three advantages of the performed balloon-based isotopic measurements over the more conventional satellite- or airplane-based measurements. First, the vertical speeds of the Jimu balloons are restrained to 10 to 15 m/min, providing higher temporal-resolution measurements compared to airplane-based profiles. Second, buoyancy is the only driving force for ascent, thus avoiding interference from mechanical vibrations with the instruments. Third, the in situ observation system directly reflects air mass advection via wind flow when the buoyancy force is weaker than advection. Prior to our study, very few airplane vertical isotopic profiles were available worldwide since the 1950s (45–51), along with a few satellite-derived vertical isotopic profiles over the AWTs (52, 53). These data provided valuable information to elucidate the moisture processes that affect the hydroclimate state in the troposphere and lower stratosphere (54–57), particularly in coastal regions (58–62).

Our in situ observations for water vapor stable isotopes ($\delta^{18}O$ and δD) and the corresponding meteorological parameters were initiated at Lulang from November 25, 2017, to December 3, 2017, using a tethered balloon with a volume of 1,200 m^3. The balloon carried a Picarro L2130i cavity-ring down spectroscopy (CRDS) and corresponding meteorological instruments, from 3,335 m a.s.l. to 5,245 m a.s.l. A new tethered balloon with a volume of 2,300 m^3 carried the same Picarro instrument to make measurements from 3,335 m a.s.l. to 6,200 m a.s.l. at Lulang from January 15 to January 25, and from 3,335 m a.s.l. to 6,305 m a.s.l. from April 18 to April 30, 2019. The same measurements were recorded at Nam Co between 4,730 m a.s.l. and 7,003 m a.s.l. from May 16 to June 2, 2019. We achieved 32 ascending-and-descending vertical profiles, totaling 90 h, with typical takeoff times after 22:00 local time (14:00 UTC), spanning 10 pm to 10 am for each duration (*SI Appendix*, Fig. S1).

The Picarro L2130i analyzer was installed in a temperature-controlled nacelle. The inlet line consisted of a 1/4-inch outer diameter Swagelok stainless steel tube and was heated to thermostabilized at 45 °C by a self-regulating heat trace. To prevent tubing wall effects by minimizing the adhesiveness between the tubing wall and the water molecules, we used a 1.5 m stainless steel tube between the inlet of the atmospheric water vapor and the measuring cell. A Parker pump (H085-11) flushed ambient air into the analyzer at a flow rate of 3 L min^{-1}. The response times for $\delta^{18}O$, δD, and H_2O for ambient air were less than 10 s during the field measurements. Due to the longer response time at lower humidity levels and air pressure that led to an increased memory effect during upward movement, the constant ascending velocity of the balloon and the nacelle was controlled at 10 to 15 m/min and measurements presented in this study were for an average time of 60 s. The data acquisition rate was 1 Hz. The air pressure was ~540 hPa at 5,255 m a.s.l. At these sites, $\delta^{18}O_v$ and δD_v were measured simultaneously on the same water vapor parcel by the Picarro L2130i, and the second-order parameter d-excess$_v$ was calculated by its conventional definition (d-excess$_v$ = $\delta D_v - 8 \times \delta^{18}O_v$). All measurements were calibrated with respect to Vienna Standard Mean Ocean Water - Standard Light Antarctic Precipitation (VSMOW2-SLAP2).

Calibration and Uncertainties for Water Vapor Measurements. The calibration was performed using a Picarro standard delivery module (SDM) with two liquid isotope working standards ($\delta^{18}O = -10.09‰$, $\delta D = -70.12‰$; $\delta^{18}O = -29.71‰$, $\delta D = -226.71‰$) independently for ground-based pre- and post-flight calibrations. The calibrations were run immediately after the Picarro L2130i was installed on the balloon, before launching and after landing (~ every 12 h). Calibration protocols followed those successfully used in Greenland as detailed by Steen-Larsen (63). To quantify the mixing ratio dependency of isotopic compositions of water vapor (named humidity-response calibration), two standards were measured at different mixing levels spanning 1,000 to 21,000 ppmv for 30 mins at each level (*SI Appendix*, Fig. S13 *A* and *B*). The measurements during the first 15 mins and the last 1 min were deleted to avoid preserving data with memory effects. Previous studies suggest that typical Allan deviations for $\delta^{18}O$ and δD were less than 0.1‰ for a mixing ratio higher than 15,000 ppmv for the Picarro L2130i (64, 65) and the drift of humidity measurements is less than 50 ppmv each month (29). Thus, the measured intervals of mixing ratio above

15,000 ppmv are larger than those in 1,000 to 15,000 ppmv. The mixing ratio measurements were corrected at the laboratory using a dew point generator and were stable even in humidity less than 2000 ppmv during the field-based calibrations with the SD less than 120 ppmv. Due to the large variability of ambient air humidity, regular calibration at three mixing ratios spanning the ambient air measurements with a duration of 25 min each were applied to ensure that the bias was correctly removed. Before launching, one calibration run was performed with both standards at mixing ratio of ~20,000, 12,000, and 6,000 ppmv, with the lowest mixing ratio adjusted to 4,000 or 2,000 ppmv depending on ambient air conditions. The same calibration was repeated after landing. To avoid the loss of measurement accuracy, we measured ambient air at least 30 mins after each calibration before launching. The linear regression calculated by daily standard measurements against their true values were applied to calibrate the ambient air measurements to the VSMOW2-SLAP2 scale. No significant drift within the calibration period was found with SD less than 0.11‰d^{-1} for $\delta^{18}O$ and 0.42‰d^{-1} for δD among the flight days. The humidity-response calibration and normalization to VSMOW-SLAP were applied for all the isotopic measurements without drift correction. The precision of the standard measurements with mixing ratios spanning 2,000 to 21,000 ppmv during the field campaign are 0.06‰ for $\delta^{18}O$ and 0.18‰ for δD, which are increased to 0.15‰ for $\delta^{18}O$ and 0.52‰ for δD with the mixing ratio below 2,000 ppmv. The uncertainties of the standard measurements with mixing ratio between 2,000 ppmv and 21,000 ppmv during the field campaign are 0.26‰ for $\delta^{18}O$ and 1.48‰ for δD. The larger uncertainties of standard measurements (0.89‰ for $\delta^{18}O$ and 5.5‰ for δD) are observed with mixing ratio below 2,000 ppmv.

Concurrent with the vertical profile measurements, ground-based isotopic measurements ($\delta^{18}O_{sv}$ and δD_{sv}) were set up at the field camps. These provided a continuous surface dataset at a 1 Hz resolution, matching the sampling rate of the tethered-balloon platform. A Picarro L2130i analyzer was installed in a container with stable temperature (15 ± 1 °C). The inlet downward was connected to a 4 m long stainless-steel tubing (1/4 inch diameter) heated to 45 °C. A KNF pump flushed ambient air into the analyzer at a flow rate of 11.5 L min^{-1}. Water vapor isotopic measurements were normalized to the VSMOW-SLAP scale. The calibration procedure was similar to that for the water vapor isotopic measurements on the balloon. To obtain the humidity-isotope response function, two standards with the same isotopic values as those used in the balloon-based Picarro were measured at humidity levels from 2,000 to 15,000 ppmv on 8th to 9th January, 10th to 12th April, and 16th to 17th May 2019, depending on the mixing ratios in the ambient air. The different response functions for δD and $\delta^{18}O$ were obtained as a function of humidity (*SI Appendix*, Fig. S13 *c*, *d*). The calibration involved daily runs of two known standards at three levels for 30 mins each and encompassing ambient air humidity. The calibration measurements were made simultaneously for the Picarro instruments in the balloon platform and the surface container during the field campaigns. The precision of the standard measurements with a mixing ratio between 2,000 and 15,000 ppmv during the field campaign is 0.05‰ for $\delta^{18}O$ and 0.22‰ for δD. The uncertainties of the standard measurements with a mixing ratio between 2,000 and 15,000 ppmv during the field campaign are 0.17‰ for $\delta^{18}O$ and 0.79‰ for δD.

Meteorological Observations. Simultaneous meteorological data were measured by two sensors on the balloon: a Vaisala (HMP155, at 1 s intervals) sensor positioned near the water vapor inlet, and a sounding meteorograph placed 4 m away from the Vaisala sensor, outside the control cabinet, which were rising or landing with the tethered balloon during in situ observations. Ground-based meteorological observations were completed, including air temperature, relative humidity, pressure, and winds, using a Campbell automatic weather station (ClimaVUE50). To coincide with the isotopic measurements, all the data are calculated as one-minute averages with error bars. The daily atmospheric reanalysis winds and specific humidity (*q*) for the period 1978–2018 from the ERA5 reanalysis data were used to calculate the average moisture flux pattern (https://cds.climate.copernicus.eu/).

Isotope Simulations. Simulations of the atmosphere circulation with the isotope-enabled ECHAM6-wiso model were used to explore the vertical variations of atmospheric water vapor stable isotopes, moisture flux, and evapotranspiration flux as well as westerly jet locations during the observation period. The simulations were performed with a horizontal model grid size of ~0.9x0.9° and 95 vertical levels (T127L95). The model is nudged to ERA5 reanalysis (66) to ensure the realism of the simulated large-scale atmospheric circulation on 6-h time steps during December 2017- June 2019. The detailed treatment of water stable isotopes in this model is based on Cauquoin and Werner (2021) (17) and Cauquoin et al. (2019) (67). The vertical simulations of atmospheric water vapor stable isotopes and specific humidity together with winds (u, v, and omega) from the surface to ~6,500 m a.s.l. (400 hPa) were extracted from the nearest grid cell encompassing our in situ locations covering the duration of our observations. A detailed comparison of δD_v, d-excess$_v$, and *q* between simulations and our observations in both surface time series and vertical profiles are provided in *SI Appendix*. The agreement between in situ observations and simulations supports confidence in the use of the model outputs to understand large-scale advections and daily variations over the AWTs. The model-data comparison for surface δD_v and d-excess$_v$ suggests that the model may underestimate surface evapotranspiration, possibly related to the representation of the land surface characteristics. Systematic biases in vertical isotope profiles of the simulations could arise from incomplete representations of dehydration/Rayleigh distillation, or unresolved topographic influences in the model.

Rayleigh Model, MBL Mixing Model, and Mixed Cloud Isotopic Model. We followed methods according to those of Worden et al. (2007) (68) to simulate the closed Rayleigh distillation and rain evaporation processes.

The Mixed Cloud Isotopic Model (MCIM) is used to estimate the effect of SST on formation of a moist air mass, without mixing between the moist air mass and the outside air, by describing the isotopic evolution at the water phase transition with varied liquid proportions inside the clouds (69).

For all the vertical observations of δD_v, we estimated the mixing variations of atmospheric water vapor, considering the influence of the atmospheric boundary layer based on a water isotopic Marine Boundary Layer (MBL) model (34). Despite the strong evidence for westerlies/Indian monsoon sources marked by low-δD/high-δD and high-d-excess/low-d-excess vapor to the southern AWTs' upper troposphere, we considered a range of other sources that might influence the isotopic composition of atmospheric vapor during our observation to calculate the mixing line. Vapor derived from meltwater or sublimation from snow is unlikely to be a major source to the atmosphere due to the small precipitation or melt amount in winter and spring. Vapor derived from the western Siberia land surface (70) (7 g/kg for *q*, −25‰ for $\delta^{18}O$, −190‰ for δD) as well as evapotranspiration vapor from the land surface covered by a large number of forests at Lulang may be significant sources in the winter. Evaporated water from the Nam Co may be a possible source, given that the lake is a warm pool after sunset in May, with water temperatures of ~2.5 to ~8 °C depending on the depth of the lake (44). This vapor is expected to have enriched isotopic composition (−6.98‰ for $\delta^{18}O$, −70.9‰ for δD) (46). We use these vapor stable isotopes and mixing models to account for influences of moisture from different sources on variations in vapor stable isotopes during our observational periods in Fig. 4.

Data, Materials, and Software Availability. The in-situ data used to obtain the conclusions in this paper is available in Zenodo repository at https://doi.org/10.5281/zenodo.19812974 (71). ECHAM6-wiso data are available in Zenodo repository at https://doi.org/10.5281/zenodo.19813762 (72).

ACKNOWLEDGMENTS. The challenging measurements of water vapor isotopes over the AWTs would not have been possible without the many operational and technical staff who supported researchers, including technicians, engineers, project managers, and station administrators. We acknowledge M.L. Zhu, Deji, M.L. Chen, F. Li, Z.Y. Wang, J.L. Li, D. Dai, Y.L. Yang, and S. Yang, who helped complete the field work. We thank M. Davis for editing the English writing. We also thank Q.H. Zhang, L.X. Wang, Q. Wang, D.H. Zhang, Y.M. Qin, Y.S. Li, X.W. Wang, X.J. Zhang, H.B. Luo, and R.C. Zhu, who participated in the implementation of the tethered balloons. We thank the staff at the South-East Tibetan Plateau Station for integrated observation and research of the alpine environment and at the Nam Co Station for Multisphere Observation and Research, CAS, for setting up the tethered balloon. This work was funded by "The Second Tibetan Plateau Scientific Expedition and Research" project (Grant Nos. 2024QZKK0400 and 2019QZKK0208), the Key Research and Development and Transformation Project of the Tibet Science and Technology Program (Grant no. XZ202501ZY0081), the Strategic Priority Research Program of Chinese Academy of Sciences (Grant No.

XDA20100300), and the National Natural Science Foundation of China (Grant No. 41922002).

Author affiliations: [a]State Key Laboratory of Tibetan Plateau Earth System, Environment and Resources, Institute of Tibetan Plateau Research, Chinese Academy of Sciences, Beijing 100101, China; [b]Laboratoire des Sciences du Climat et de l'Environnement (LSCE), CEA–CNRS–UVSQ–Paris-Saclay–IPSL, UMR8212, Université Paris Saclay, Orme des Merisiers, Gif-sur-Yvette 91191, France; [c]Alfred Wegener Institute, Helmholtz Centre for Polar and Marine Research, Bremerhaven D-27570, Germany; [d]Byrd Polar and Climate Research Center and School of Earth Sciences, Ohio State University, Columbus, OH 43210; [e]Geophysical Institute, University of Bergen, Bergen 5020, Norway; [f]Institute of Industrial Science, The University of Tokyo, Kashiwa 153-8505, Japan; [g]Byrd Polar and Climate Research Center and Department of Geography, Ohio State University, Columbus, OH 43210; [h]Aerospace Information Research Institute, Chinese Academy of Sciences, Beijing 100094, China; [i]Key Laboratory of Coast and Island Development of Ministry of Education, School of Geography and Ocean Science, Nanjing University, Nanjing 210023, China; and [j]National Space Science Center, Chinese Academy of Sciences, Beijing 100190, China

Author contributions: J.G. designed research; M.W., J.J., L.T., M.C., H.C.S.-L., A.C., Z.H., R.C., T.Z., Y.L., G.C., B.X., G.W., and M.H. performed research; T.Y. advised on research design and data analysis; V.M.-D. conducted statistical analysis and discussed the results; M.W. and A.C. ran the ECHAM6-wiso simulations; J.J., L.T., M.C., H.C.S.-L., and H.M. assisted with data interpretation and presentation; E.M.-T. discussed data analysis and presentation; Z.H., T.Z., and R.C. responsible for management of the tethered balloon during the flights; Y.L. and G.C. performed the isotopic models outputs; H.P. provided the standards of water stable isotopes; and J.G. wrote the paper.

Reviewers: R.S.B., University of Massachusetts; and A.S., Technische Universität Braunschweig.

The authors declare no competing interest.

1. J. Gao, T. Yao, V. Masson-Delmotte, H. C. Steen-Larsen, W. Wang, Collapsing glaciers threaten Asia's water supplies. *Nature* **565**, 19–21 (2019).
2. T. Yao *et al.*, The imbalance of the Asian water tower. *Nat. Rev. Earth Environ.* **3**, 618–632 (2022), 10.1038/s43017-022-00299-4.
3. R. Schiemann, D. Luthi, C. Schar, Seasonality and interannual variability of the westerly jet in the Tibetan Plateau. *J. Clim.* **22**, 2940–2957 (2009).
4. J. Curio, F. Maussion, D. Scherer, A 12-year high-resolution climatology of atmospheric water transport over the Tibetan Plateau. *Earth Syst. Dynam.* **6**, 109–124 (2015).
5. J. C. H. Chiang, M. J. Herman, K. Yoshimura, I. Y. Fung, Enriched East Asian oxygen isotope of precipitation indicates reduced summer seasonality in regional climate and westerlies. *Proc. Natl. Acad. Sci. U.S.A.* **117**, 14745–14750 (2020).
6. Ipcc, The ocean and cryosphere in a changing climate (2022), 10.1017/9781009157964.
7. J. Curio, D. Scherer, Seasonality and spatial variability of dynamic precipitation controls on the Tibetan Plateau. *Earth Syst. Dyn.* **7**, 767–782 (2016).
8. T. Molg, F. Maussion, D. Scherer, Mid-latitude westerlies as a driver of glacier variability in monsoonal High Asia. *Nat. Clim. Change* **4**, 68–73 (2014).
9. T. D. Yao *et al.*, Different glacier status with atmospheric circulations in Tibetan Plateau and surroundings. *Nat. Clim. Change* **2**, 663–667 (2012).
10. T. D. Yao *et al.*, The imbalance of the Asian water tower. *Nat. Rev. Earth Environ.* **3**, 618–632 (2022).
11. P. Zhao *et al.*, The third atmospheric scientific experiment for understanding the earth-atmosphere coupled system over the Tibetan Plateau and its effects. *Bull. Am. Meteorol. Soc.* **99**, 757–776 (2018).
12. J. C. H. Chiang, M. J. Herman, K. Yoshimura, I. Y. Fung, Enriched East Asian oxygen isotope of precipitation indicates reduced summer seasonality in regional climate and westerlies. *Proc. Natl. Acad. Sci. U.S.A.* **117**, 14745–14750 (2020), 10.1073/pnas.1922602117.
13. T. D. Yao *et al.*, A review of climatic controls on delta 18O in precipitation over the Tibetan Plateau: Observations and simulations. *Rev. Geophys.* **51**, 525–548 (2013).
14. J. Gao, V. Masson-Delmotte, C. Risi, Y. He, T. Yao, What controls precipitation delta O-18 in the southern Tibetan Plateau at seasonal and intra-seasonal scales? A case study at Lhasa and Nyalam *Tellus Series B-Chem. Phys. Meteorol.* **65**, 21043 (2013).
15. I. D. Clark, P. Fritz, Environmental Isotopes in Hydrogeology (CRC Press, Boca Raton, 1997).
16. J. Galewsky *et al.*, Stable isotopes in atmospheric water vapor and applications to the hydrologic cycle. *Rev. Geophys.* **54**, 809–865 (2016), 10.1002/2015rg000512.
17. A. Cauquoin, M. Werner, High-resolution nudged isotope modeling with ECHAM6-Wiso: Impacts of updated model physics and ERA5 reanalysis data. *J. Adv. Model. Earth Syst.* **13**, e2021MS002532 (2021).
18. J. Che, P. Zhao, Characteristics of the summer atmospheric boundary layer height over the Tibetan Plateau and influential factors. *Atmos. Chem. Phys.* **21**, 5253–5268 (2021).
19. M. Chen *et al.*, Temporal variations of stable isotopic compositions in atmospheric water vapor on the Southeastern Tibetan Plateau and their controlling factors. *Atmos. Res.* **303**, 107328 (2024), 10.1016/j.atmosres.2024.107328.
20. D. Dai *et al.*, Continuous monitoring of the isotopic composition of surface water vapor at Lhasa, southern Tibetan Plateau. *Atmos. Res.* **264**, 105827 (2021).
21. L. Tian *et al.*, Control of seasonal water vapor isotope variations at Lhasa, southern Tibetan Plateau. *J. Hydrol.* **580**, 124237 (2020).
22. Z. Zhao *et al.*, Black carbon aerosol and its radiative impact at a high-altitude remote site on the southeastern Tibet Plateau. *J. Geophys. Res.: Atmos.* **122**, 5515–5530 (2017).
23. D. Zannoni *et al.*, Non-equilibrium fractionation factors for D/H and 18O/16O During oceanic evaporation in the North-West Atlantic Region. *J. Geophys. Res.: Atmos.* **127**, e2022JD037076 (2022).
24. H. Bailey *et al.*, Arctic sea-ice loss fuels extreme European snowfall. *Nat. Geosci.* **14**, 283–288 (2021).
25. S. Acharya, X. Yang, T. Yao, D. Shrestha, Stable isotopes of precipitation in Nepal Himalaya highlight the topographic influence on moisture transport. *Quaternary Int.* **565**, 22–30 (2020).
26. A. L. Putman, R. P. Fiorella, G. J. Bowen, Z. Cai, A global perspective on local meteoric water lines: Meta-analytic insight into fundamental controls and practical constraints. *Water Resour. Res.* **55**, 6896–6910 (2019).
27. R. Fu *et al.*, Short circuit of water vapor and polluted air to the global stratosphere by convective transport over the Tibetan Plateau. *Proc. Natl. Acad. Sci. U.S.A.* **103**, 5664–5669 (2006).
28. W. Dansgaard, Stable isotopes in precipitation. *Tellus* **16**, 436–468 (1964).
29. A. Bailey *et al.*, Isotopic measurements in water vapor, precipitation, and seawater during EUREC4A. *Earth Syst. Sci. Data* **15**, 465–495 (2023).
30. Y. Li, F. Aemisegger, A. Riedl, N. Buchmann, W. Eugster, The role of dew and radiation fog inputs in the local water cycling of a temperate grassland during dry spells in central Europe. *Hydrol. Earth Syst. Sci.* **25**, 2617–2648 (2021).
31. K. E. Samuels-Crow, J. Galewsky, Z. D. Sharp, K. J. Dennis, Deuterium excess in subtropical free troposphere water vapor: Continuous measurements from the Chajnantor Plateau, northern Chile. *Geophys. Res. Lett.* **41**, 8652–8659 (2014).
32. C. Frankenberg *et al.*, Dynamic processes governing lower-tropospheric HDO/H2O ratios as observed from space and ground. *Science* **325**, 1374–1377 (2009).
33. D. Noone *et al.*, Determining water sources in the boundary layer from tall tower profiles of water vapor and surface water isotope ratios after a snowstorm in Colorado. *Atmos. Chem. Phys.* **13**, 1607–1623 (2013).
34. M. Benetti *et al.*, A Framework to Study Mixing Processes in the Marine Boundary Layer Using Water Vapor Isotope Measurements. *Geophys. Res. Lett.* **45**, 2524–2532 (2018).
35. M. Berkelhammer *et al.*, Surface-atmosphere decoupling limits accumulation at Summit, Greenland. *Sci. Adv.* **2**, e1501704 (2016).
36. J. Jiang *et al.*, Precipitation regime changes in High Mountain Asia driven by cleaner air. *Nature* **623**, 544–549 (2023).
37. Q. Zhang *et al.*, Oceanic climate changes threaten the sustainability of Asia's water tower. *Nature* **615**, 87–93 (2023).
38. J. Jouzel *et al.*, Validity of the temperature reconstruction from water isotopes in ice cores. *J. Geophys. Res.-Oceans* **102**, 26471–26487 (1997).
39. V. Masson-Delmotte *et al.*, Grip deuterium excess reveals rapid and orbital-scale changes in Greenland moisture origin. *Science* **309**, 118–121 (2005).
40. W. Yu *et al.*, Influences of relative humidity and Indian monsoon precipitation on leaf water stable isotopes from the southeastern Tibetan Plateau. *Geophys. Res. Lett.* **41**, 7746–7753 (2014).
41. E. Liang, Y. Wang, D. Eckstein, T. Luo, Little change in the fir tree-line position on the southeastern Tibetan Plateau after 200 years of warming. *New Phytol.* **190**, 760–769 (2011).
42. J. Wang *et al.*, Spatial and temporal variations in water temperature in a high-altitude deep dimictic mountain lake (Nam Co), central Tibetan Plateau. *J. Great Lakes Res.* **45**, 212–223 (2019).
43. R. Witt *et al.*, Biogeochemical evidence for freshwater periods during the Last Glacial Maximum recorded in lake sediments from Nam Co, south-central Tibetan Plateau. *J. Paleolimnol.* **55**, 67–82 (2016).
44. S. Kang, Y. Yi, Y. Xu, B. Xu, Y. Zhang, Water Isotope framework for lake water balance monitoring and modelling in the Nam Co Basin, Tibetan Plateau. *J. Hydrol.: Reg. Stud.* **12**, 289–302 (2017).
45. D. H. Ehhalt, N. Roper, H. E. Moore, Vertical profiles of nitrous oxide in the troposphere. *J. Geophys. Res.* **80**, 1653–1655 (1975).
46. S. D. Gedzekman, Deuterium in water vapor above the atmospheric boundary layer. *Tellus B: Chem. Phys. Meteorol.* **40**, 134–147 (2017).
47. H. He, R. B. Smith, Stable isotope composition of water vapor in the atmospheric boundary layer above the forests of New England. *J. Geophys. Res.: Atmos.* **104**, 11657–11673 (1999).
48. W. Pollock, L. E. Heidt, R. Lueb, D. H. Ehhalt, Measurement of stratospheric water vapor by cryogenic collection. *J. Geophys. Res.* **85**, 5555–5568 (1980).
49. M. Tsujimura *et al.*, Vertical distribution of stable isotopic composition in atmospheric water vapor and subsurface water in grassland and forest sites, eastern Mongolia. *J. Hydrol.* **333**, 35–46 (2007).
50. A. Zahn, E. Christner, P. F. J. van Velthoven, A. Rauthe-Schöch, C. A. M. Brenninkmeijer, Processes controlling water vapor in the upper troposphere/lowermost stratosphere: An analysis of 8 years of monthly measurements by the IAGOS-CARIBIC observatory. *J. Geophys. Res.: Atmos.* **119**, 11,505–511,525 (2014).
51. C. R. Webster, A. J. Heymsfield, Water isotope ratios D/H, 18O/16O, 17O/16O in and out of clouds map dehydration pathways. *Science* **302**, 1742–1745 (2003).
52. W. J. Randel *et al.*, Global variations of HDO and HDO/H2O ratios in the upper troposphere and lower stratosphere derived from ACE-FTS satellite measurements. *J. Geophys. Res.: Atmos.* **117**, D06303 (2012).
53. J. E. Lee *et al.*, Asian monsoon hydrometeorology from TES and SCIAMACHY water vapor isotope measurements and LMDZ simulations: Implications for speleothem climate record interpretation. *J. Geophys. Res.: Atmos.* **117**, D15112 (2012).
54. S. M. Khaykin *et al.*, Persistence of moist plumes from overshooting convection in the Asian monsoon anticyclone. *Atmos. Chem. Phys.* **22**, 3169–3189 (2022).
55. K. S. Rozmiarek *et al.*, An unmanned aerial vehicle sampling platform for atmospheric water vapor isotopes in polar environments. *Atmos. Measur. Tech.* **14**, 7045–7067 (2021).
56. D. Henze, D. Noone, D. Toohey, Detection of dilution due to turbulent mixing vs. precipitation scavenging effects on biomass burning aerosol concentrations using stable water isotope ratios during ORACLES. *Atmos. Chem. Phys.* **23**, 15269–15288 (2023).
57. T. F. Hanisco *et al.*, Observations of deep convective influence on stratospheric water vapor and its isotopic composition. *Geophys. Res. Lett.* **34**, L04814 (2007).
58. C. Dyroff *et al.*, Airborne in situ vertical profiling of HDO / $H_2^{16}O$ in the subtropical troposphere during the MUSICA remote sensing validation campaign. *Atmos. Meas. Tech.* **8**, 2037–2049 (2015).
59. B. Stevens *et al.*, EUREC4A. *Earth Syst. Sci. Data* **13**, 4067–4119 (2021).
60. H. Sodemann *et al.*, The stable isotopic composition of water vapour above Corsica during the HyMeX SOP1 campaign: Insight into vertical mixing processes from lower-tropospheric survey flights. *Atmos. Chem. Phys.* **17**, 6125–6151 (2017).
61. R. L. Herman *et al.*, Aircraft validation of Aura Tropospheric Emission Spectrometer retrievals of HDO/H2O. *Atmos. Measur. Tech.* **7**, 3127–3138 (2014).
62. M. Schneider *et al.*, Empirical validation and proof of added value of MUSICA's tropospheric δD remote sensing products. *Atmos. Measur. Tech.* **8**, 483–503 (2015).

63. H. C. Steen-Larsen *et al.*, Continuous monitoring of summer surface water vapor isotopic composition above the Greenland Ice Sheet. *Atmos. Chem. Phys.* **13**, 4815–4828 (2013).
64. F. Aemisegger *et al.*, Measuring variations of δ18O and δ2H in atmospheric water vapour using two commercial laser-based spectrometers: An instrument characterisation study. *Atmos. Measur. Tech.* **5**, 1491–1511 (2012).
65. Y. Weng, A. Touzeau, H. Sodemann, Correcting the impact of the isotope composition on the mixing ratio dependency of water vapour isotope measurements with cavity ring-down spectrometers. *Atmos. Meas. Tech.* **13**, 3167–3190 (2020).
66. H. Hersbach *et al.*, The ERA5 global reanalysis. *Q. J. R. Meteor. Soc.* **146**, 1999–2049 (2020).
67. A. Cauquoin, M. Werner, G. Lohmann, Water isotopes–Climate relationships for the mid-Holocene and preindustrial period simulated with an isotope-enabled version of MPI-ESM. *Clim. Past* **15**, 1913–1937 (2019).
68. J. Worden, D. Noone, K. Bowman, T. Tropospheric Emission Spectrometer Science, C. Data, Importance of rain evaporation and continental convection in the tropical water cycle. *Nature* **445**, 528–532 (2007).
69. L. Merlivat, J. Jouzel, Global Climatic Interpretation of the Deuterium-Oxygen-18 Relationship for Precipitation. *J. Geophys. Res.-Oceans* **84**, 5029–5033 (1979).
70. V. Bastrikov *et al.*, Continuous measurements of atmospheric water vapour isotopes in western Siberia (Kourovka). *Atmos. Measur. Tech.* **7**, 1763–1776 (2014).
71. J. Gao. Atmospheric water vapor stable isotopes on the Asian Water Towers [Dataset]. Zenodo. https://doi.org/10.5281/zenodo.19812974. Deposited 4 April 2023.
72. A. Cauquoin, M. Werner, ECHAM6-wiso T127L95 nudged data around the Asian Water Towers [Dataset]. Zenodo. https://doi.org/10.5281/zenodo.19813762. Deposited 27 April 2026.